# Wind Stress Dependence on Ocean Surface Velocity: Implications for Mechanical Energy Input to Ocean Circulation

THOMAS H. A. DUHAUT AND DAVID N. STRAUB

*Atmospheric and Oceanic Sciences, McGill University, Montreal, Quebec, Canada*

(Manuscript received 18 August 2004, in final form 12 July 2005)

ABSTRACT

It is pointed out that accounting for an ocean surface velocity dependence in the wind stress $\tau$ can lead to a significant reduction in the rate at which winds input mechanical energy to the geostrophic circulation. Specifically, the wind stress is taken to be a quadratic function of $\mathbf{U}_a - \mathbf{u}_o$, where $\mathbf{U}_a$ and $\mathbf{u}_o$ are the 10-m wind and ocean surface velocity, respectively. Because $|\mathbf{U}_a|$ is typically large relative to $|\mathbf{u}_o|$, accounting for a $\mathbf{u}_o$ dependence leads only to relatively small changes in $\tau$. The change to the basin-averaged wind power source, however, is considerably larger. Scaling arguments and quasigeostrophic simulations in a basin setting are presented. They suggest that the power source (or rate of energy input) is reduced by roughly 20%–35%.

## 1. Introduction

Ocean circulation models often approximate the surface wind stress $\tau$ exerted by the atmosphere on the ocean as being a function of the atmospheric winds alone. For example, a simple parameterization would have that $\tau = \tau_0$, where $\tau_0 \equiv \rho_a c_d |\mathbf{U}_a| \mathbf{U}_a$. Here, $\mathbf{U}_a$ is the 10-m atmospheric wind, $\rho_a$ is the density of air at sea level, and $c_d$ is constant to leading order (e.g., Hellerman and Rosenstein 1983). This formulation neglects a surface ocean velocity $\mathbf{u}_o$ dependence in $\tau$, and it is widely appreciated that $\tau_1 \equiv \rho_a c_d |\mathbf{U}_a - \mathbf{u}_o| (\mathbf{U}_a - \mathbf{u}_o)$ represents an improvement. Nevertheless, $\tau_0$ is commonly used for the simple reason that wind speeds are typically large relative to current speeds, so that $\tau_1 - \tau_0$ is small over most of the ocean. Use of $\tau_1$ in place of $\tau_0$ has, however, been shown to lead to significant improvements in simulations of the tropical Atlantic Ocean (Pacanowski 1987). More recently, Luo et al. (2005) found similar improvements in the tropical Pacific Ocean. They use the $\tau_1$ formulation in a coarse-resolution coupled model and find a significant reduction (improvement) in the westward extension of the "cold tongue" along the equator.

*Corresponding author address:* Thomas Duhaut, Atmospheric and Oceanic Sciences, 805 Sherbrooke W., McGill University, Montreal, QC H3A 2K6, Canada.
E-mail: tduhau@po-box.mcgill.ca

Scatterometer measurements of $\tau$ are based on a backscatter signal associated with surface capillary waves. As such, the ocean surface velocity dependence is implicitly accounted for in these measurements. Using buoy data, Kelly et al. (2001) show this more explicitly. Specifically, they show scatterometer-derived wind stress over the tropical Pacific to be a function of air–sea velocity difference. In the South Equatorial Current the $\mathbf{u}_o$ dependence leads to a decrease of approximately 20% in the median amplitude of the stress, with local modifications being as large as 50%. They go on to comment that changes to the wind stress curl can be expected to be even larger.

Over much of the midlatitude ocean, current speeds are small relative to atmospheric winds. Outside of boundary currents, therefore, the direct effect of the $\mathbf{u}_o$ dependence in $\tau_1$ is typically smaller. Nevertheless, clear signatures of oceanic currents are seen in scatterometer data. Using National Aeronautics and Space Administration (NASA) Scatterometer (NSCAT) data and $\mathbf{u}_o$-dependent formulations for $\tau$, Cornillon and Park (2001) were able to deduce ocean currents over warm-core Gulf Stream rings that compared well with ADCP measurements. Milliff and Morzel (2001) used 9-month averages of NSCAT data to show a dipole-like structure in the wind stress curl across ocean currents. Similarly, the Gulf Stream is clearly evident in 4-yr averages of the wind stress curl obtained from the Quick Scatterometer (QuikSCAT) (Chelton et al. 2004). They

argue this to be partially due to a feedback between sea surface temperature and wind stress, but also to a $\mathbf{u}_o$ dependence in $\tau$—similar to that in $\tau_1$. The basic idea is that, even though the correction to $\tau$ is small, the correction to the curl is much larger. This follows since $\mathbf{u}_o$ is associated with smaller horizontal length scales than is $\mathbf{U}_a$.

A more extreme modification to $\tau_0$ has been introduced by Bye (Bye 1986; Bye and Wolff 1999). In this formulation, the stress is a function of $\mathbf{U}_a - (1/\varepsilon)\mathbf{u}_o$, where $\varepsilon \equiv (\rho_{\text{air}}/\rho_{\text{water}})^{1/2}$.[1] A typical value of $\varepsilon$ is about 1/30. Thus, a 0.2 m s$^{-1}$ ocean current would have as large an effect on $\tau$ as would a 6 m s$^{-1}$ wind. As mentioned above, scatterometer data support instead a formulation more similar to $\tau_1$. We therefore focus on this.

We are interested in the rate at which the winds add mechanical energy to the geostrophic circulation. This has been referred to in the literature alternately as the kinetic energy input (Crawford and Large 1996) and the power input (Scott 1999). The latter conforms with usage in engineering and will be adopted here. We define the wind power input (per unit area) to be $P \equiv \mathbf{u}_o \cdot \tau$. In mks, $P$ has units of kilograms per second cubed, such that an area integral of $P$ has units of Joules per second. In what follows, we neglect wind power source to high-frequency oscillations, such as near-inertial motions. This has been addressed elsewhere in the literature (e.g., Large and Crawford 1995; Crawford and Large 1996).

Our main point is that the ocean surface velocity dependence in $\tau_1$ has a relatively large influence on spatial averages of $P$. For the case in which $\mathbf{u}_o$ is taken to be the geostrophic component of the surface velocity, $P$ can be thought of as the rate of working by the winds on the geostrophic circulation.[2] Estimates of this have been made using satellite altimetry data and various estimates of the wind stress (Wunsch 1998; Scott 1999). Wunsch finds the time-mean power input to be dominated by the time-mean zonal wind stress multiplied by the mean zonal surface currents. Terms involving transients or meridional velocity components play a relatively minor role. He also shows the Southern Ocean to be a region in which $P$ is particularly large and speculates that a local dissipation of this power would imply enhanced diapycnal mixing in the region. Scott emphasizes that while errors in $\mathbf{u}_o$ related to uncertainty in the geoid make local estimates of $P$ uncertain, this uncertainty is decreased upon spatial averaging since the geoid errors can be considered uncorrelated with $\tau$. He also shows there to be considerable temporal variability in area-averaged estimates of $P$ (e.g., over the North Pacific). In neither of these studies, however, is explicit use made of the systematic dependence of $\tau$ on $\mathbf{u}_o$. In other words, they (effectively) consider $\mathbf{u}_o \cdot \tau_0$ rather than $\mathbf{u}_o \cdot \tau_1$. Our point is that use of $\tau_1$ leads to a considerable reduction of spatial averages of $P$.

Below, simple scaling arguments are made to support this claim, and in section 3, model evidence is presented. Specifically, we revisit the classic quasigeostrophic (QG) double-gyre problem, but using $\tau_1$ rather than $\tau_0$ as forcing. While the QG system is clearly an oversimplification, we nonetheless feel that it is useful. Because it is relatively inexpensive to integrate we can better resolve the mesoscale and thus minimize an aphysical energy sink that occurs when the kinetic-energy-containing and dissipation length scales are comparable. Nonetheless, since we are arguing that use of $\tau_1$ in place of $\tau_0$ makes a significant difference to the actual ocean, it is important that our idealized model simulations be in a realistic regime. We accomplish this by choosing a standard bottom friction parameter, for which various model statistics (e.g., rms velocity) correspond roughly to what is observed in the midlatitude ocean.

We also consider a twin experiment designed to illustrate possible pitfalls that might arise in applying a scatterometer-derived $\tau$ in modeling ocean circulation. Specifically, a scatterometer-derived wind stress (which implicitly takes into account the ocean velocity dependence) might lead to spurious energy sources when applied to models. This could occur since the model surface velocity field will differ from the actual velocity field. We conclude with a brief discussion.

## 2. Scaling arguments

We are interested in comparing estimates of the basin-averaged wind power input with the geostrophic circulation using the two formulations of the wind stress: $\tau_0$ and $\tau_1$. Let $P_0$ and $P_1$ be the power input based on $\tau_0$ and $\tau_1$, respectively, and let $P_{\text{diff}}$ and $\tau_{\text{diff}}$ correspond to $P_0 - P_1$ and $\tau_0 - \tau_1$. We would like to compare basin-averaged estimates of $P_0$ and $P_{\text{diff}}$. Three simplifying assumptions are made:

(i) $|\mathbf{U}_a|$ is large relative to $|\mathbf{u}_o|$,
(ii) $\mathbf{U}_a$ has large horizontal length scales, and
(iii) $\mathbf{u}_o$ can be thought of as the sum of $\mathbf{u}_{\text{basin}}$ and $\mathbf{u}_{\text{mesoscale}}$,

[1] In Bye's formulation, $\mathbf{U}_a$ is the geostrophic wind above the bottom boundary layer.

[2] Strictly speaking, use of the geostrophic approximation for the $\mathbf{u}_o$ appearing explicitly in the scalar product does not imply that a geostrophic $\mathbf{u}_o$ need also be used in the definition of $\tau_1$. We will nonetheless make this assumption. As discussed below, we do not believe that this simplification changes our principal conclusions.

where $\mathbf{u}_{\text{basin}}$ is weak and characterized by large spatial scales and $\mathbf{u}_{\text{mesoscale}}$ is more energetic, with smaller horizontal scales. In other words,

$$|\mathbf{U}_a| \gg |\mathbf{u}_{\text{mesoscale}}| \gg |\mathbf{u}_{\text{basin}}| \quad \text{and} \quad L_a \sim L_{\text{basin}} \gg L_{\text{mesoscale}},$$

where the $L$s represent horizontal length scales.

These assumptions are broadly consistent with both theory and observations. For example, it is common in ocean circulation theory to think of $\mathbf{u}_o$ as being decomposed along the lines that we suggest. Here $\mathbf{u}_{\text{mesoscale}}$ can be thought of as corresponding to features such as boundary currents, their seaward extensions, rings, and mesoscale eddies. These are all fast relative to the interior basin-scale Sverdrup drift and slow relative to the wind speed. Moreover, our assumption that $L_a \sim L_{\text{basin}} \gg L_{\text{mesoscale}}$ is consistent with the usual assumption that midlatitude gyres are driven primarily by large-scale winds.

Given these assumptions, $\tau_0$ can be expected to project well onto $\mathbf{u}_{\text{basin}}$ and poorly onto $\mathbf{u}_{\text{mesoscale}}$. For example, in the classic double-gyre problem, only the gravest Fourier mode projects onto the forcing. More generally,

$$\langle P_0 \rangle \sim \rho_a c_d u_{\text{basin}} U_a^2, \tag{1}$$

where the angle brackets denote basin averaging and $u_{\text{basin}}$ and $U_a$ are typical values of $|\mathbf{u}_{\text{basin}}|$ and $|\mathbf{U}_a|$.

By contrast, $\tau_{\text{diff}}$ projects well onto $\mathbf{u}_o$. Because of this and because kinetic energy is dominated by the mesoscale,

$$\langle P_{\text{diff}} \rangle \sim \rho_a c_d U_a u_{\text{mesoscale}}^2. \tag{2}$$

Hence,

$$\frac{\langle P_{\text{diff}} \rangle}{\langle P_0 \rangle} \sim \left( \frac{u_{\text{mesoscale}}}{U_a} \right) \left( \frac{u_{\text{mesoscale}}}{u_{\text{basin}}} \right). \tag{3}$$

Plugging in $U_a \sim 10$ m s$^{-1}$, $u_{\text{mesoscale}} \sim 0.2$ m s$^{-1}$, and $u_{\text{basin}} \sim 0.02$ m s$^{-1}$ as rough estimates of the three speeds, one gets a ratio of 0.2. It thus appears that accounting for an ocean velocity dependence in $\tau$ can lead to a reduction of the wind power input by about 20%.

Note that both $\langle P_0 \rangle$ and $\langle P_{\text{diff}} \rangle$ are positive. That $\langle P_0 \rangle$ is positive simply says that the large-scale winds do work on the oceans. Indeed, if this were not the case, it would be senseless to talk of a wind-driven circulation. That $\langle P_{\text{diff}} \rangle$ is positive implies that the $\mathbf{u}_o$ dependence in $\tau_1$ acts to reduce the power source. That this should be the case is shown below.

It is useful to first simplify $\tau_1$, taking into account that $|\mathbf{u}_o| \ll |\mathbf{U}_a|$. Note that

$$|\mathbf{U}_a - \mathbf{u}_o| \approx |\mathbf{U}_a| - \mathbf{u}_o \cdot \mathbf{i}, \tag{4}$$

where $\mathbf{i}$ is a unit vector pointing in the direction of $\mathbf{U}_a$. In other words, to leading order, only the component of $\mathbf{u}_o$ aligned with the wind affects $|\mathbf{U}_a - \mathbf{u}_o|$. Next, using (4) and the definition of $\tau_1$, one gets

$$\tau_{\text{diff}} \equiv \tau_0 - \tau_1 \approx \rho_a c_d |\mathbf{U}_a| \mathbf{u}_o + \rho_a c_d (\mathbf{u}_o \cdot \mathbf{i}) \mathbf{U}_a, \tag{5}$$

where quadratic terms in $\mathbf{u}_o$ have been neglected. The first term on the rhs is equivalent to a linear "Stommel" drag on the surface ocean velocity, with the caveat that the drag coefficient is proportional to $|\mathbf{U}_a|$. The second term can be thought of as an additional drag on the component of $\mathbf{u}_o$ that is parallel to $\mathbf{U}_a$. Thus, $P_{\text{diff}} \equiv \mathbf{u}_o \cdot \tau_{\text{diff}}$ is given by

$$P_{\text{diff}} \approx \rho_a c_d |\mathbf{U}_a| \left[ |\mathbf{u}_o|^2 + (\mathbf{u}_o \cdot \mathbf{i})^2 \right]. \tag{6}$$

Note that both terms on the rhs of (6) are positive-definite. They can be thought of as $|\mathbf{U}_a|$-weighted averages of $|\mathbf{u}_o|^2$ and $(\mathbf{u}_o \cdot \mathbf{i})^2$, respectively. Since $|\mathbf{u}_{\text{mesoscale}}| \gg |\mathbf{u}_{\text{basin}}|$, both terms scale like the rhs of (2). Therefore, our estimate above that the power source can be reduced by 20% or so can be thought of as a lower estimate (i.e., since both terms scale as such and the two are additive).

## 3. Model

It seems useful to examine the relative sizes of $P$ and $P_{\text{diff}}$ in a numerical simulation. We consider the classic double-gyre problem in a three-layer quasigeostrophic ocean. The domain is taken to be square and the depth is uniform. Forcing assumes a wind stress of the form $\tau_1$, with $\mathbf{U}_a$ specified such that $\tau_0$ corresponds to the classic double-gyre stress:

$$\tau_0 = (\tau_0^x, \tau_0^y) = -\tau_0 \left[ \cos\left( \frac{2\pi y}{L} \right), 0 \right]. \tag{7}$$

Here $y$ varies between 0 and $L$, $\tau_0$ is 0.1 N m$^{-2}$, and $\rho_a c_d = 10^{-3}$ kg m$^{-3}$. This gives 10 m s$^{-1}$ as the peak value for $|\mathbf{U}_a|$.

As mentioned in the introduction, this is obviously highly idealized. A bottom friction parameter is chosen so that the overall solution has characteristics that are comparable to those typical of ocean gyres (cf. Table 1 and related discussion). Use of the idealized dynamics and domain allows us to achieve a higher resolution than would otherwise be feasible and to illustrate the effect of $\tau_{\text{diff}}$ in a familiar, well-studied setting.

TABLE 1. Various statistics from the simulation; $u$ and $v$ refer to upper-layer zonal and meridional velocities, respectively, and the transports give the gyre strengths integrated over the two upper layers. Time means were taken from an 80-yr average following the initial spinup.

| Quantity | Value | Type |
|---|---|---|
| $u_{\max}$ (m s$^{-1}$) | ~2.4 | Snapshot |
| $v_{\max}$ (m s$^{-1}$) | ~2.6 | Snapshot |
| $u_{\text{rms}}$ (m s$^{-1}$) | ~0.25 | Snapshot |
| $v_{\text{rms}}$ (m s$^{-1}$) | ~0.23 | Snapshot |
| $T_{\text{subtropical}}$ (Sv*) | 72 | Mean |
| $T_{\text{subpolar}}$ (Sv) | 66 | Mean |
| $T_{\text{Sverdrup}}$ (Sv) | 31 | Linear theory |
| $\bar{u}_{\max}$ (m s$^{-1}$) | 0.8 | Mean |
| $\bar{v}_{\max}$ (m s$^{-1}$) | 2.5 | Mean |

* 1 Sv $\equiv 10^6$ m$^3$ s$^{-1}$.

Model equations are fairly standard:

$$\frac{D}{Dt}\left[\nabla^2\psi_1 + \beta y + \frac{f_0^2}{g_1 H_1}(\psi_2 - \psi_1)\right] = \frac{\mathbf{k}\cdot(\boldsymbol{\nabla}\times\tau_1)}{\rho_0 H_1} - A\nabla^6\psi_1,$$

$$\frac{D}{Dt}\left[\nabla^2\psi_2 + \beta y + \frac{f_0^2}{g_1 H_2}(\psi_1 - \psi_2) + \frac{f_0^2}{g_2 H_2}(\psi_3 - \psi_2)\right] = -A\nabla^6\psi_2, \quad \text{and}$$

$$\frac{D}{Dt}\left[\nabla^2\psi_3 + \beta y + \frac{f_0^2}{g_2 H_3}(\psi_2 - \psi_3)\right] = -A\nabla^6\psi_3 - r\nabla^2\psi_3, \tag{8}$$

where $r$ and $A$ correspond to bottom and biharmonic friction coefficients. The amplitude of the two baroclinic zero-potential-vorticity modes (i.e., modes for which relative and stretching vorticity sum to zero) are also calculated at each time step (McWilliams 1977). Here $r$ was taken to be $10^{-7}$ s$^{-1}$, corresponding to a 115-day spindown time for kinetic energy in the abyssal layer and $A$ was taken to be $5 \times 10^9$ m$^4$ s$^{-1}$. With a resolution of 8 km, this ensured one point in the inner viscous boundary layer.[3] Other model parameters were as follows: $g_1 = 3 \times 10^{-2}$ m s$^{-2}$, $g_2 = 1.5 \times 10^{-2}$ m s$^{-2}$, $H_1 = 300$ m, $H_2 = 700$ m, $H_3 = 4000$ m, $\beta = 2 \times 10^{-11}$ m$^{-1}$ s$^{-1}$, and $f_0 = 10^{-4}$ s$^{-1}$. This gave first and second baroclinic Rossby radii of 40 and 22 km, respectively. The domain width was 4000 km and horizontal grid was 501[2]. Numerical details can be found in Cummins and Mysak (1988).

Results from three simulations are reported: S1–S3, where S1 is our reference experiment. It is forced using $\tau_1$ as described above and will serve a dual purpose. It will first be used to verify the scaling presented in section 2 and will also be considered as "truth" in a twin experiment, which compares S1 with S2.

Simulation S2 is initialized from a snapshot of S1 at a time following the initial spinup. A small random perturbation is then added to the upper layer and integration continues in tandem for the two simulations. Forcing for S2 uses the $\tau_1$ field derived from S1. Since the dynamics are chaotic, we expect the two solutions to diverge. That is, although snapshots from S2 may look qualitatively similar to snapshots from S1, they will differ in detail. Therefore, correlations that should exist between the stress and the (S2) velocity field are compromised. The idea is to mimic the effect of using a wind stress taken directly from scatterometer data for use in a more realistic model.[4] Such a wind stress field implicitly contains information about the actual currents, but these will differ (at least in detail) from the modeled currents. Therefore, the systematic damping effect of the $\mathbf{u}_o$ dependence in $\tau$ is compromised. Because of this, it is conceivable that S2 may actually be worse (farther from S1) than S3, for which $\tau_0$ defines the forcing—thus making S3 analogous to a general circulation model forced with a stress derived from atmospheric wind data alone.

Milliff et al. (1999) considered a similar comparison between scatterometer-enhanced and National Centers for Environmental Prediction (NCEP) wind forcing. They focus on large-scale features (i.e., they use a coarse-resolution model). Also, in their study, the $\mathbf{u}_o$ dependence in the forcing was implicit. As such, their comparison is roughly analogous to one between our experiments S2 and S3. Here, we are primarily interested in effects relating to the mesoscale and to an explicit $\mathbf{u}_o$ dependence in the forcing.

We take the point of view that energy dissipation by lateral friction should be minimal. Because quasigeostrophic turbulence does not cascade energy forward to small scales, scale-selective dissipation should not dissipate energy in the high-resolution, low-viscous-coefficient limit. In practice, however, obtaining a clean separation between the energy-containing and dissipation parts of the spectrum is difficult. A biharmonic

[3] For numerical stability, one generally requires a minimum of one point in the "Munk" layer. For biharmonic dissipation, $L_{\text{"Munk"}} = (A/\beta)^{1/5}$. We used the more stringent condition that there should be one grid point in the "inner viscous layer" (see Pedlosky 1996). Here, this scale is given by $L_{\text{inner}} \sim L_{\text{"Munk"}}(L_{\text{"Munk"}}/L_{\text{Rhines}})^{1/4}$. We estimate this to be about 9 km.

[4] An obvious difference is that in our twin experiment, the "observed" stress is known everywhere, whereas complete coverage for scatterometer winds is only available after the satellite completes several orbits.

(rather than harmonic) representation of lateral friction increases the scale selectivity and hence minimizes dissipation by lateral friction at the scale of the energy-containing eddies. Boundary conditions are taken to correspond to free slip. Specifically, we take $\nabla^2\psi = \nabla^4\psi = 0$ at the walls.

One might also take the point of view that the lateral dissipation term represents the effect not only of unresolved quasigeostrophic modes, but also of other dynamics that have been filtered explicitly by the quasigeostrophic approximation. To the extent that a dissipation scheme is meant to represent these effects, one can argue that the viscous coefficient should not be lowered as resolution is increased and that the lateral dissipation term should dissipate energy. At low Rossby number, however, energy exchanges between geostrophic and gravity modes are weak (Ford et al. 2000). In parts of the domain, however, the Rossby number is arguably $O(1)$. In these regions, it seems possible that energy transfers to forward-cascading modes may be significant (M.-P. Lelong 2004, personal communication; Straub 2003). Additionally, the energetics can be affected by geostrophic flow over rough topography, which allows for a transfer of energy out of the geostrophic modes. These effects are not considered here.

## 4. Results

After an initial spinup, our reference simulation, S1, reached a statistical equilibrium. Figure 1 shows snapshots and a time average of the upper-layer streamfunction. We were surprised to find that long time averages yielded solutions that were asymmetric about $y = L/2$. Given the symmetry of the forcing and our use of quasigeostrophic dynamics, one would normally expect the time-mean streamfunction to be antisymmetric about $y = L/2$. Of course, it is well known that asymmetric steady solutions exist in similar problems (e.g., Cessi and Ierley 1995; Jiang et al. 1995). When dissipation parameters are weak, however, these solutions are generally unstable, and we were surprised to find asymmetric long time means in simulations that were strongly turbulent. We confirmed that this aspect of the solution is not related to our use of $\tau_1$: simulations forced with $\tau_0$ showed similar long time means (not shown).[5]

[5] As a consistency check, we verified that the code could also produce asymmetric statistical equilibria with the opposite sense of asymmetry. Specifically, we restarted the code after flipping (and inverting the sign of) the streamfunctions about the line $y = L/2$—so that an enlarged subtropical gyre resulted. After 100 model years, the time mean was similar to that shown in Fig. 1a, but with the opposite sense of asymmetry.

One might have anticipated that the solutions could vacillate between parts of the phase space corresponding to two different unstable asymmetric solutions. Indeed, a tendency for the system to move back and forth between multiple "preferred regimes" has been noted in similar problems (McCalpin and Haidvogel 1996). Here, it seems instead that the system develops either an enlarged subpolar or subtropical gyre and does not flip back and forth between the two. Rather, the degree, but not the sign of the asymmetry varies in time. Representative snapshots are shown in Fig. 1.

Clearly the persistence of this asymmetry in a (moderately) high "Reynolds" number limit merits closer scrutiny; however, as it appears unrelated to whether $\tau_0$ or $\tau_1$ is used as forcing, we consider further discussion to be beyond the scope of this note.

Apart from this asymmetry, the gross features of the solution are more or less what one might expect: a time-mean Sverdrup flow in the interior, western boundary currents feeding into a meandering seaward extension, an eddy-rich region of nearly homogeneous potential vorticity in the middle layer, and so on. These features are fairly standard and discussions can be found in Pedlosky (1996) and the references therein. Other characteristics of our simulation are found in Table 1. Except for a time-mean meridional velocity that is too large, model statistics seem reasonably close to observations and to simulations in more realistic settings (e.g., Smith et al. 2000; Capotondi et al. 1995). The model time-mean meridional velocity was 2.5 m s$^{-1}$ and is located adjacent to the western boundary. This is to be related to our choice of a free-slip boundary condition. Although this is unrealistically large, it does not significantly affect the results. Specifically, although contributions from the western boundary currents to $P_{\text{diff}}$ are significant, they remain relatively small. Maximum instantaneous velocities (both meridional and zonal) are also around 2.5 m s$^{-1}$. This is somewhat (but not exceedingly) larger than observed values, which are typically under 2 m s$^{-1}$. Other statistics, such as the rms and maximum time-mean zonal velocities were similar to what is typically found in model experiments. Because our model statistics do not correspond precisely to those of the actual ocean, the size of $P_{\text{diff}}$ reported here may be different—mostly likely slightly larger—than its actual value. That said, we feel the model statistics are close enough to observations such that our estimates of $P_{\text{diff}}$ are comparable to what would be found in more expensive and realistic simulations.

Figure 2 shows time series of various terms in the energy balance. Plotted is the power source, $\langle P_1 \rangle$, and the sinks due to bottom friction and lateral friction. The net power source is balanced primarily by bottom fric-

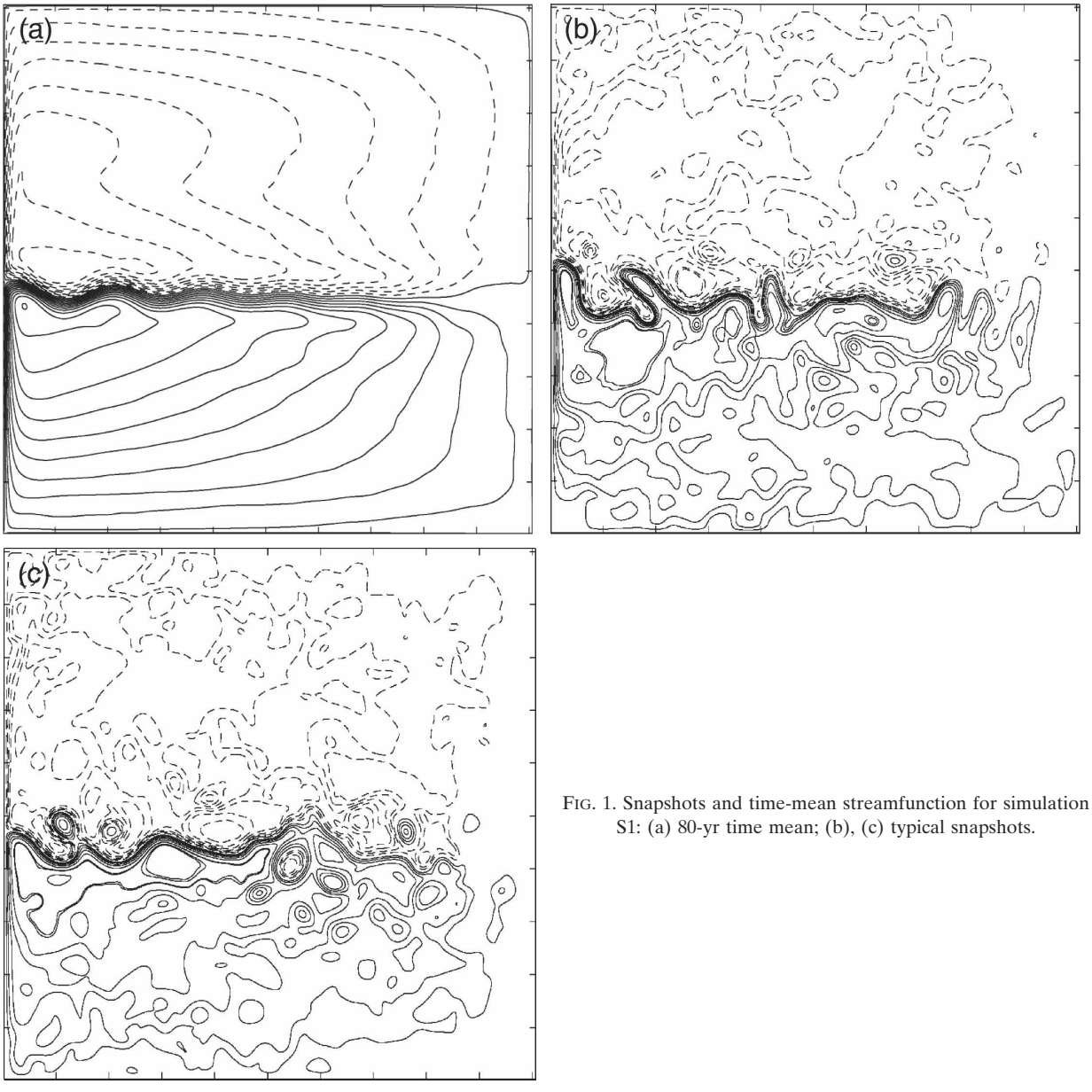


FIG. 1. Snapshots and time-mean streamfunction for simulation S1: (a) 80-yr time mean; (b), (c) typical snapshots.

tion, so that we are in the regime of interest in the sense that lateral dissipation plays a secondary role in the energetics. Also shown (top curve) is $\langle P_0 \rangle$ (calculated using $\tau_0$ and the $\mathbf{u}_o$ from S1; see also Fig. 5 later). The difference between $\langle P_0 \rangle$ and $\langle P_1 \rangle$ gives a measure of how strongly the $\mathbf{u}_o$ dependence in $\tau$ is reducing the net power input. Of the power put in by $\tau_0$, roughly one-third is "dissipated" by the $\mathbf{u}_o$ dependence in $\tau$.

Figure 3 shows the spatial structure of $P_{\text{diff}}$ plotted on a log scale. In Figs. 3a and 3b, respectively, values below 0.1 and 0.001 times the maximum value are not shown. Clearly, the midlatitude jet makes a dominant contribution to $\langle P_{\text{diff}} \rangle$, with the western boundary currents making a smaller contribution. For example, the eight grid points nearest the western boundary account for about 9% of $\langle P_{\text{diff}} \rangle$ in the snapshot.

Because smaller values of $P_{\text{diff}}$ occupy most of the domain, it is not immediately obvious whether they make a sizable contribution to the integral. Direct calculation indicates, however, that they do. For example, values above the threshold for Fig. 3b, but below that for Fig. 3a (i.e., between 0.1% and 10% of the maximum value) account for about 30% of the total. (Values between 0.1% and 1% of the maximum account for about 10% of the total.) It thus appears that roughly one-third of $\langle P_{\text{diff}} \rangle$ is associated with features that are

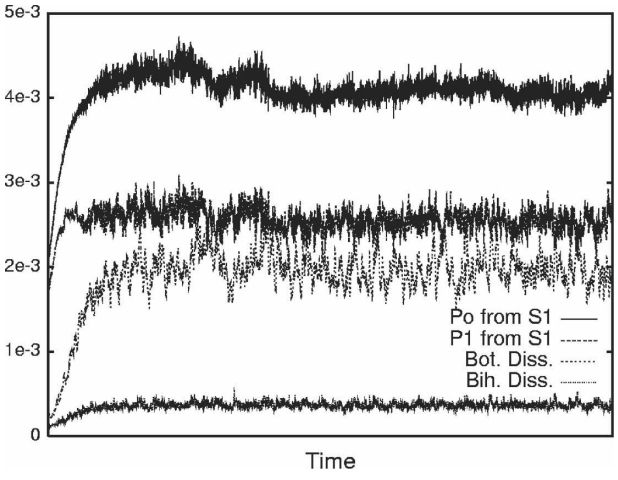


FIG. 2. Time series of various terms in the energy equation (W $m^{-2}$) for simulation S1: $P_0$ (top curve), $P_1$ (second from top), bottom dissipation (third from top), and lateral dissipation (bottom).

not directly linked to the boundary currents and jet (e.g., to mesoscale eddies and rings, as opposed to the jet).

It is also of interest to decompose $\langle P_{\text{diff}} \rangle$ into contributions associated with the time-mean and transient velocity fields. Doing this, we find the $P_{\text{diff}}$ field associated with the time-mean $\mathbf{u}_o$ to account for about one-third of the total, with the transient contribution making up the remainder. Bye and Wolff (1999) make a similar point. They find the effect of $\tau_B$ to be greater in the presence of eddies.[6]

Note that our finding that transients make a dominant contribution to $\langle P_{\text{diff}} \rangle$ does not contradict the finding by Wunsch (1998) that time averages of $\langle P \rangle$ are dominated by the time-mean zonal stress and velocity. As pointed out, the stress assumed by Wunsch did not include a $\mathbf{u}_o$ dependence: it corresponds to $\tau_0$. Hence, the relevant $\langle P \rangle$ is $\langle P_0 \rangle$. We took $\tau_0$ to be both zonal and steady. Thus, essentially by definition, our $\langle P_0 \rangle$ is given by $(\overline{u})(\overline{\tau_0^x})$,[7] where overbars here represent time averages. This is actually somewhat larger than $(\overline{u})(\overline{\tau_1^x})$, since the time-mean zonal velocity affects $P_{\text{diff}}$. Nonetheless, our results agree with those of Wunsch in that $(\overline{u})(\overline{\tau_1^x})$ dominates not only $\langle P_0 \rangle$, but also $\langle P_1 \rangle$. On the other hand, transients make a dominant contribution to $\langle P_{\text{diff}} \rangle$.

The dissipative effect of the $\mathbf{u}_o$ dependence in $\tau$ can also be seen from vorticity dynamics. Because $\mathbf{U}_a$ has large horizontal scales relative to $\mathbf{u}_o$, the curl of $\tau_{\text{diff}}$ is generally larger than the curl of $\tau_0$ (Fig. 4). Moreover, this correction to the wind stress curl is clearly anticorrelated with the surface vorticity. For instance, in the anticyclonic gyre, the curl over the boundary current

[6] This result uses a time-averaged $\mathbf{u}_o$ in the definition of $\tau_{\text{Bye}}$; see the discussion in their section 7a.

[7] Alternatively, it is equal to the amplitude of the $(k_x, k_y) = (0, 2\pi/L)$ Fourier mode of the time-mean $u$, multiplied by $0.5\tau_0$ [cf. Eq. (7)].

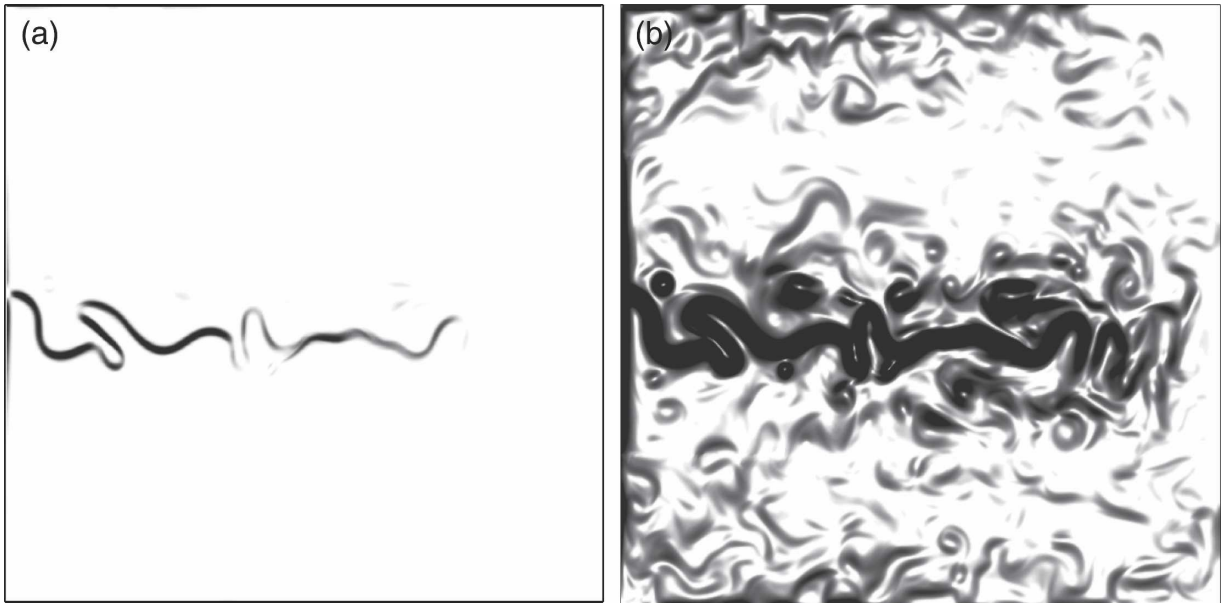


FIG. 3. The $P_{\text{diff}}$ field for the snapshot in Fig. 1b plotted on a log scale: (a) only values above 0.1 times the maximum are shown; (b) values above 0.001 times the maximum are shown. The portion of the field visible in (b) but not in (a) accounts for about 30% of the total.

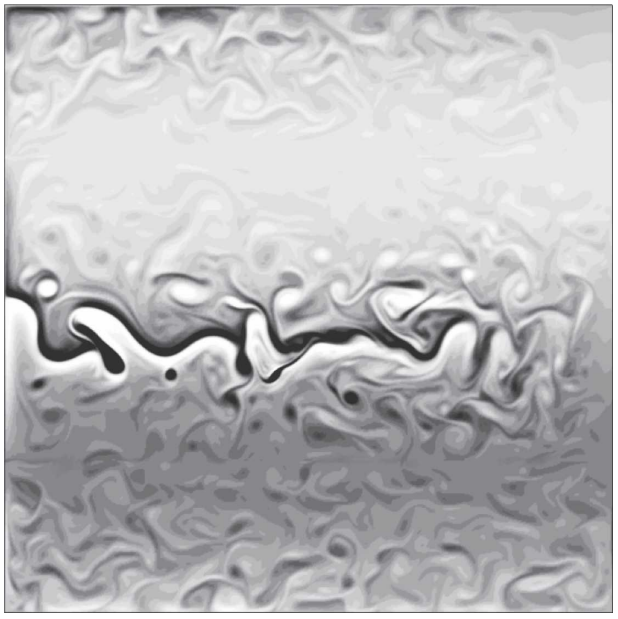

FIG. 4. Wind stress curl $[\mathbf{k} \cdot (\nabla \times \tau_1)]$ for the snapshot corresponding to Fig. 1b. Lighter shades correspond to cyclonic forcing.

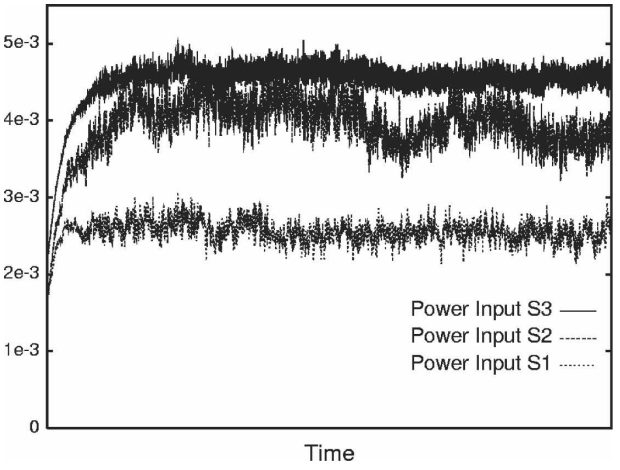


FIG. 5. Time series of $\langle P \rangle$ (W m$^{-2}$) for experiments S1 (bottom curve), S2 (middle), and S3 (top).

and its extension is positive. As such, it acts to remove anticyclonic vorticity from these currents. Similarly, the analogous forcing in the cyclonic gyre is anticyclonic. Chelton et al. (2004) made a similar comment with respect to their 4-yr mean wind stress curl data over the North Atlantic. As was the case for the power input, transients allow for an even greater damping of the vorticity. This can be seen from time-mean and transient contributions to the enstrophy sink associated with the $\mathbf{u}_o$ dependence in $\tau$:

$$\text{Sink} = -\int \zeta \mathbf{k} \cdot (\nabla \times \tau_{\text{diff}})\, dx\, dy\,, \tag{9}$$

where the integral is over the basin and $\zeta$ is relative vorticity. We calculated this using both instantaneous and time-mean fields for $\zeta$ and $\mathbf{u}_o$ and found the sink based on the instantaneous fields to be larger by a factor of about 4.

Figure 5 shows time series of $\langle P \rangle$ for the three simulations, where $\langle P_{S3} \rangle$ is slightly larger than $\langle P_{S2} \rangle$ and both are large relative to $\langle P_{S1} \rangle$. Also, $\langle P_{S2} \rangle$ shows stronger variability. That $\langle P_{S3} \rangle$ is large relative to $\langle P_{S1} \rangle$ is consistent with our interpretation of the $\mathbf{u}_o$ dependence in $\tau_1$ as a damping effect. Note also that $\langle P_{S3} \rangle$ is larger (by about 7%) than $\langle P_0 \rangle$ plotted in Fig. 2 (i.e., for simulation S1). This is associated with an increase in the large-scale velocity field when $\tau_0$ is used as forcing. Specifically, the $(k_x, k_y) = (0, 2\pi/L)$ mode of the time-averaged zonal velocity is larger by about 7%. Therefore, we conclude that use of $\tau_1$ results in a reduction of the power source in two ways. First, the basin-scale circulation is modified so as to decrease $P_0$. This is seen by comparing the top curves in Figs. 2 and 5, but see also Scott and Straub (1998). Second, and more important, $P_{\text{diff}}$ systematically reduces the net power source (as seen from comparing the top two curves in Fig. 2).

That $\langle P_{S2} \rangle$ is slightly smaller than $\langle P_{S3} \rangle$ means that the "scatterometer derived" winds used in S2 led to a slight reduction in the wind power source. We interpret this as follows. The model (S2) velocity field reasonably mimics the "actual" (S1) velocity field at large scales, but does less well at smaller scales. Therefore, the "observed" stress corrects large-scale, but not small-scale, features in $\tau$. Since $P_{\text{diff}}$ is mainly associated with the mesoscale, however, the net result is only a weak damping. This is detailed further below.

Figure 6 shows time-averaged convolutions of $\mathbf{u}_o \cdot \tau_{\text{diff}}$ for S1 and S2, plotted as functions of horizontal wavenumber. For S1, features corresponding to wavenumbers 5–20 dominate $P_{\text{diff}}$. The largest value is at wavenumber 12, corresponding to a length scale of about 53 km. The kinetic energy spectrum (not shown) has a shoulder at approximately the same wavenumber. In other words, $P_{\text{diff}}$ is dominated by the same length scales that contain the bulk of the kinetic energy.

For simulation S2, the convolution follows that of S1 up to wavenumber 3, implying that the S1 and S2 velocity fields agree up to wavenumber 3. At higher horizontal wavenumbers, modeled (S2) and observed (S1) velocities do not match, and the power sink is much reduced. For S2, it was not obvious to us a priori whether mesoscale features might lead to a negative contribution to $\langle P_{\text{diff}} \rangle$ (i.e., to an increase in the power input).

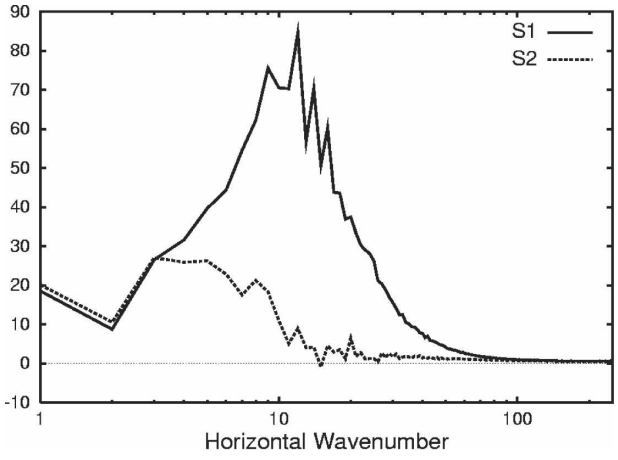


FIG. 6. Convolution of $\mathbf{u}_o \cdot \tau_{\text{diff}}$ for simulations S1 and S2, plotted as a function of horizontal wavenumber. Values are multiplied by the horizontal wavenumber so that the area under the curve corresponds to the power sink. Units are arbitrary.

That is, if S1 and S2 velocities were sufficiently decorrelated, then one would expect (minus) $\tau_{\text{diff}}$—calculated using S1 velocities—to act essentially as a random forcing term. Negative values were seen at some horizontal wavenumbers in individual snapshots; however, they disappear in time averages. Instead, the time average simply shows a reduced sink. This is because the mesoscale velocity fields in the two simulations remain somewhat correlated. For example, S2 velocities tend, on average, to be eastward at the position of the S1 jet, that is, where $-\tau_{\text{diff}}$ is large and westward. Hence, $P_{\text{diff}}$ tends to act as a sink, although a weaker one than would be the case if the magnitude of the (eastward) velocity were systematically large where $-\tau_{\text{diff}}$ is large and westward.

## 5. Discussion

Simple scaling arguments and a three-layer quasigeostrophic model were used to make the point that accounting for a $\mathbf{u}_o$ dependence in the wind stress can significantly alter the energetics of wind-driven ocean circulation. For our reference simulation, the net effect on the wind power input was to reduce it by about one-third. The average change in the wind stress was considerably less: the rms value for $|\tau_{\text{diff}}|$ was about 7% of the rms $|\tau_0|$. Local changes in $\tau$, however, were larger, and changes to the power input where $\langle\tau_{\text{diff}}\rangle$ is large accounts for most (roughly 1/3) of the change in $\langle P\rangle$.

Various other feedbacks between the ocean state and the forcing were not considered, and these will surely be important to a complete picture. Thomas and Rhines (2002) point out that finite vorticity effects can lead to dramatic changes in the Ekman pumping field, and surely this also alters the energetics. Chelton et al. (2004) point out that sea surface temperature gradients also affect the wind stress curl (and divergence); however, they estimate this effect to be secondary with respect to the $\mathbf{u}_o$ dependence in $\tau$ in boundary current regimes. Note also that we interpreted the $\mathbf{u}_o$ in $\tau_1$ as corresponding to the leading-order quasigeostrophic velocity. More correctly, $\tau_1$ would also depend on the Ekman velocity. However, if one accepts that the relevant Ekman velocity is, to leading order, at some fixed angle to $\mathbf{U}_a$ (i.e., as in the classical theory), then it would have length scales similar to $L_a$. As such, the implied modifications to $\tau_1$ would not project well onto the mesoscale velocity and our scaling arguments would be unaffected.

As emphasized by Bye (1986), it seems possible that the surface wave field also plays a significant role. Bye's formulation, $\tau_B$, is based on a similarity assumption and amounts to an $O(1)$ change (relative to $\tau_0$) in the stress itself (i.e., not just in derived quantities such as $P$ or $\nabla \times \tau$). Note however that wave effects also enter into more standard formulations of $\tau$. For example, $c_d$ is not strictly constant, but depends on sea state. In the $\tau_0$ formulation, Hellerman and Rosenstein (1983) consider that $c_d$ should increase with $|\mathbf{U}_a|$ for values greater than 6.7 m s$^{-1}$. In the $\tau_1$ formulation, this would appear as a dependence of $c_d$ on $|\mathbf{U}_a - \mathbf{u}_o|$, and would result in an increase in the effective damping of surface currents aligned with the wind, in regions of strong wind.

In addition to surface gravity waves directly affecting the air–sea momentum exchange, it is also conceivable that horizontal transport of momentum by the waves might also play a role. For example, momentum imparted to the surface waves at one location might ultimately be transferred to the general circulation at another. If so, there would result a modification of the "effective stress" acting on the general circulation. Presumably, however, this effect is small.

Last, we noted that direct application of scatterometer-derived winds to ocean general circulation models will tend to underrepresent the damping associated with the $\mathbf{u}_o$ dependence in $\tau$. This is not to say, of course, that scatterometer data cannot be used to improve our knowledge of the forcing. Clearly they contain useful information relating to $\mathbf{U}_a$ (synoptic-scale variability, etc.). We simply caution that, to the extent possible, the observed ocean velocity dependence should be removed from the stress—and be replaced with an explicit dependence of $\tau$ on the model surface velocity.

*Acknowledgments.* This work was motivated by a conversation with Chris Hughes. Funding from NSERC and CFCAS is gratefully acknowledged, as are useful comments from two anonymous reviewers.

## REFERENCES

Bye, J. A. T., 1986: Momentum and heat balance in steady coastal currents. *Estuarine Coastal Shelf Sci.,* **23,** 1–28.

——, and J.-O. Wolff, 1999: Atmosphere–ocean momentum exchange in general circulation models. *J. Phys. Oceanogr.,* **29,** 671–692.

Capotondi, A., W. R. Holland, and P. Malanotte-Rizzoli, 1995: Assimilation of altimeter data into a quasigeostrophic model of the Gulf Stream system. Part II: Assimilation results. *J. Phys. Oceanogr.,* **25,** 1153–1174.

Cessi, P., and G. R. Ierley, 1995: Symmetry-breaking multiple equilibria in quasigeostrophic, wind-driven flows. *J. Phys. Oceanogr.,* **25,** 1196–1205.

Chelton, D. B., M. Schlax, M. Freilich, and R. Milliff, 2004: Satellite measurements reveal persistent small-scale features in ocean winds. *Science,* **303,** 978–983.

Cornillon, P., and K.-A. Park, 2001: Warm core ring velocities inferred from NSCAT. *Geophys. Res. Lett.,* **28,** 575–578.

Crawford, G. B., and W. Large, 1996: A numerical investigation of resonant inertial response of the ocean to wind forcing. *J. Phys. Oceanogr.,* **26,** 873–891.

Cummins, P. F., and L. Mysak, 1988: A quasi-geostrophic circulation model of the northeast Pacific. Part I: A preliminary numerical experiment. *J. Phys. Oceanogr.,* **18,** 1261–1286.

Ford, R., M. McIntyre, and W. Norton, 2000: Balance and the slow quasimanifold: Some explicit results. *J. Atmos. Sci.,* **57,** 1236–1254.

Hellerman, S., and M. Rosenstein, 1983: Normal monthly wind stress over the World Ocean with error estimates. *J. Phys. Oceanogr.,* **13,** 1093–1104.

Jiang, S., F.-F. Jin, and M. Ghil, 1995: Multiple equilibria, periodic and aperiodic solutions in a wind-driven, double-gyre, shallow water model. *J. Phys. Oceanogr.,* **25,** 764–786.

Kelly, K. A., S. Dickinson, M. McPhaden, and G. Johnson, 2001: Ocean currents evident in satellite wind data. *Geophys. Res. Lett.,* **28,** 2469–2472.

Large, W. G., and G. Crawford, 1995: Observations and simulations of upper-ocean response to wind events during the ocean storms experiment. *J. Phys. Oceanogr.,* **25,** 2831–2852.

Luo, J.-J., S. Masson, E. Roeckner, G. Madec, and T. Yamagata, 2005: Reducing climatology bias in an ocean–atmosphere CGCM with improved coupling physics. *J. Climate,* **18,** 2344–2360.

McCalpin, J. D., and D. Haidvogel, 1996: Phenomenology of the low-frequency variability in a reduced-gravity, quasigeostrophic double-gyre model. *J. Phys. Oceanogr.,* **26,** 739–752.

McWilliams, J. C., 1977: A note on a consistent quasigeostrophic model in a multiply connected domain. *Dyn. Atmos. Oceans,* **1,** 427–441.

Milliff, R. F., and J. Morzel, 2001: The global distribution of the time-average wind stress curl from NSCAT. *J. Atmos. Sci.,* **58,** 109–131.

——, W. Large, J. Morzel, and G. Danabasoglu, 1999: Ocean general circulation model sensitivity to forcing from scatterometer winds. *J. Geophys. Res.,* **104,** 11 337–11 358.

Pacanowski, R. C., 1987: Effect of equatorial currents on surface wind stress. *J. Phys. Oceanogr.,* **17,** 833–838.

Pedlosky, J., 1996: *Ocean Circulation Theory.* Springer-Verlag, 414 pp.

Scott, R. B., 1999: Mechanical energy flux to the surface geostrophic flow using TOPEX/Poseidon data, in physics and chemistry of the earth: Part A. *Solid Earth Geod.,* **24,** 399–402.

——, and D. N. Straub, 1998: Small viscosity behavior of a homogeneous, quasi-geostrophic, ocean circulation model. *J. Mar. Res.,* **56,** 1225–1258.

Smith, R. D., M. Maltrud, F. Bryan, and M. Hecht, 2000: Numerical simulation of the North Atlantic Ocean at 1/10°. *J. Phys. Oceanogr.,* **30,** 1532–1561.

Straub, D. N., 2003: Instability of 2D flows to hydrostatic 3D perturbations. *J. Atmos. Sci.,* **60,** 79–102.

Thomas, L. N., and R. B. Rhines, 2002: Nonlinear stratified spin-up. *J. Fluid Mech.,* **473,** 211–244.

Wunsch, C., 1998: The work done by the wind on the oceanic general circulation. *J. Phys. Oceanogr.,* **28,** 2332–2340.